ARTICLE

Optimal Configuration Method for Multi-Type Reactive Power Compensation Devices in Regional Power Grid with High Proportion of Wind Power

Ying Wang[1], Jie Dang[1], Cangbi Ding[2,*], Chenyi Zheng[2] and Yi Tang[2]

[1]Central China Branch of State Grid, Wuhan, 430077, China

[2]School of Electrical Engineering, Southeast University, Nanjing, 211100, China

*Corresponding Author: Cangbi Ding. Email: dcb19960926@163.com

ABSTRACT

As the large-scale development of wind farms (WFs) progresses, the connection of WFs to the regional power grid is evolving from the conventional receiving power grid to the sending power grid with a high proportion of wind power (WP). Due to the randomness of WP output, higher requirements are put forward for the voltage stability of each node of the regional power grid, and various reactive power compensation devices (RPCDs) need to be rationally configured to meet the stable operation requirements of the system. This paper proposes an optimal configuration method for multi-type RPCDs in regional power grids with a high proportion of WP. The RPCDs are located according to the proposed static voltage stability index (VSI) and dynamic VSI based on dynamic voltage drop area, and the optimal configuration model of RPCDs is constructed with the lowest construction cost as the objective function to determine the installed capacity of various RPCDs. Finally, the corresponding regional power grid model for intensive access to WFs is constructed on the simulation platform to verify the effectiveness of the proposed method.

KEYWORDS

Wind power; reactive power compensation device; optimal configuration model; voltage stability

Nomenclature

WF	wind farm
WP	wind power
RPCD	reactive power compensation device
VSI	voltage stability index
RPCP	reactive power compensation point
RPCD	reactive power compensation device
$\dot{U}_{w}$	terminal voltage of the WF unit
$\dot{U}_{p}$	voltage at the point of grid connection
$\dot{U}_{g}$	equivalent voltage of the system
R_{w}	equivalent resistance of the transmission line and transformer
X_{w}	equivalent reactance of the transmission line and transformer
R_{g}	equivalent resistance of the power grid
X_{g}	equivalent reactance of the power grid

P_w	active power output of the wind turbine
Q_w	reactive power output of the wind turbine
CB	Capacitor Bank
STATCOM	Static Synchronous Compensator
C_{CB}	total capacitance of the CB
U_{CB}	voltage at both terminals of the CB
ω	angular frequency of the grid
Q_{STAT}	reactive power provided or absorbed by STATCOM
U_{STAT}	output voltage amplitude of STATCOM
I_{STAT}	output current amplitude of STATCOM
δ_{STAT}	phase angle of the output voltage
θ_g	phase angle of the grid voltage
a	send-out node connected to the j-th substation
A	total number of send-out nodes connected to j-th substation
$P_a + jQ_a$	power of the a-th send-out node
U_i	bus voltage vector of the i-th substation
$|U_j|$	bus voltage amplitude of substation j
Z_{ij}^*	conjugation of the mutual impedance between substations
$\tilde{S}_i$	equivalent output power of the i-th substation of the system
$S_{RTVDAI,j}(f)$	dynamic voltage drop area
M	number of adjacent nodes
F	number of check faults of the j-th voltage weak point
$I_{RTVDAI,j}$	maximum value of $S_{RTVDAI,j}(f)$ under each check fault
t'_{start}	moment when first experiences voltage drop to 80%
t'_{start}	moment when recovers above 80% of its rated value
U_{i_N}	voltage rated value of the i-th adjacent node
$u_i(t)$	voltage trajectory curve of the i-th node under the fault
C_1	unit capacity construction cost of static RPCD
C_2	unit capacity construction cost of the dynamic RPCD
Q_{c1_k}	capacity of static RPCD at the k-th point
Q_{c2_k}	capacity of dynamic RPCD at the k-th point
N_k	total number of RPCPs
U_{qN}	operation voltage rating of the q-th node
U_q	operation voltage value of the q-th node
$A_{i,set}$	threshold value of the critical transient voltage drop area
t^k_{start}	moment when voltage drops to 0.8 p.u.
t^k_{end}	moment when the voltage recovers to above 0.8 p.u.
$U^k_i(t)$	voltage trajectory curve of the i-th node
x^{t+1}_{id}	particle position after iteration
v^{t+1}_{id}	particle velocity after iteration
p^t_{id}	historical optimal solution of the particle
p^t_{gd}	global optimal solution

1 Introduction

Utilizing renewable energy for power generation is an important measure to address global climate change, among which WF, as an important renewable energy power generation mode, has a high

utilization rate of wind energy and huge development potential [1–3]. The intensive access of WFs also causes the regional power grid to change from the conventional receiving power grid to the sending power grid with a high proportion of WP [4–7]. Due to the weaker voltage-maintaining capability of the power grid where WFs are connected, instances occur where wind turbines are forced to shut down due to low voltage protection. As the output of WFs increases and fluctuates significantly, it becomes difficult to ensure the voltage quality of the regional power grid [8–11]. The influence of WFs on the voltage/reactive power of the power grid has become one of the main obstacles limiting the installed capacity of WFs, so it is urgent to carry out in-depth research on the optimal configuration method of multi-type reactive power compensation devices in power grid with a high proportion of WP [12–16].

Identifying the voltage-weak nodes of the system accurately is the first step in achieving the rational allocation of reactive power compensation devices in regional grids with intensive wind power integration. Currently, traditional methods for identifying voltage-weak nodes in power systems can be classified into static analysis methods and dynamic analysis methods [17,18]. References [19,20] utilize various static Voltage Stability Index (VSI) methods to assess grid-connected wind power systems, highlighting insufficient system reactive power support and wind turbine output as key factors in grid voltage instability. Reference [21] evaluates voltage stability in systems with increasing wind energy penetration using the P-V curve method, determining the required capacity of reactive power compensation devices at different penetration rates. Additionally, reference [22] attempts to utilize historical and real-time monitoring data to identify voltage weak nodes, which can help identify potential issues within the system and provide predictive solutions. Reference [23] combines comprehensive analysis methods with static, dynamic, and data-driven approaches, evaluating the voltage stability of the system by considering information from different aspects. This method generally provides more comprehensive and accurate results but requires more computational resources and data support.

In the planning and design stage, research on the capacity allocation of reactive power compensation devices for wind farms mainly relies on load flow analysis and sensitivity analysis to assess the system's reactive power requirements, focusing on the reactive power balance and voltage stability of the system under static conditions to determine the optimal capacity of reactive power compensation devices [24,25]. References [26,27] comprehensively consider factors such as the static and dynamic characteristics of the system, load characteristics, and wind farm operating conditions, employing multi-objective optimization or various optimization algorithms to comprehensively optimize the capacity allocation of reactive power compensation devices. This method can ensure system stability while minimizing system operating costs and reactive power losses to the greatest extent. References [28,29] utilize advanced machine learning techniques, analyzing historical and real-time monitoring data to establish optimization models for reactive power compensation device capacity considering wind farm integration and predict the system's future reactive power requirements. References [30–32] allocate reactive power according to a proportional control strategy, that is, based on the current reactive power capacity of each wind turbine unit. In addition, some scholars have proposed optimal reactive power configuration strategies based on different optimization algorithms to reduce transmission line losses and transformer losses of wind turbine units [33,34]. However, conventional methods like RPCD installation at integration points or within WFs fail to meet static and dynamic voltage stability requirements in large-scale grid-connected WF systems, necessitating reactive power configuration optimization for grid-connected WF systems.

In this paper, an optimal configuration method of multi-type RPCDs for regional power grids with a high proportion of WP is proposed. Firstly, the operation characteristics of WF groups, various RPCDs and the actual power grid in a regional power grid with a high proportion of WP are analyzed.

Secondly, static VSI and dynamic VSI under typical operation scenarios are proposed, and the voltage-weak nodes of the regional power grid are determined based on the calculation of static VSI and dynamic VSI. Thirdly, the optimal configuration model of RPCD is constructed with the objective of minimizing the construction cost of reactive power compensation devices, and the model meets the requirements of static voltage and dynamic voltage stability of the system. Finally, the proposed method is verified in the simulation model, which proves the economy and reliability of the proposed method.

2 Overall Strategy Framework

The continuous increase in installed WP capacity will result in a large number of energy bases with a high proportion of WP transmitting electricity to load centers in modern power systems, as shown in Fig. 1a. Due to the random nature of WP output and the relatively low proportion of traditional power sources with strong regulation capabilities, such as coal-fired and gas-fired units, in the transmission grids with a high proportion of WP, it is difficult to suppress the impact of large fluctuations in WP output on the voltage, power angle, and frequency fluctuations of various nodes in the transmission grid. In particular, the operation conditions of node voltages not only affect the operational conditions of various WFs in the transmission grid, but also directly impact the transmission capacity of the outgoing channels in the transmission grid. Therefore, this paper focuses on the transmission grid with a high proportion of WP and proposes an efficient and economical method for optimizing the allocation of multi-type RPCDs.
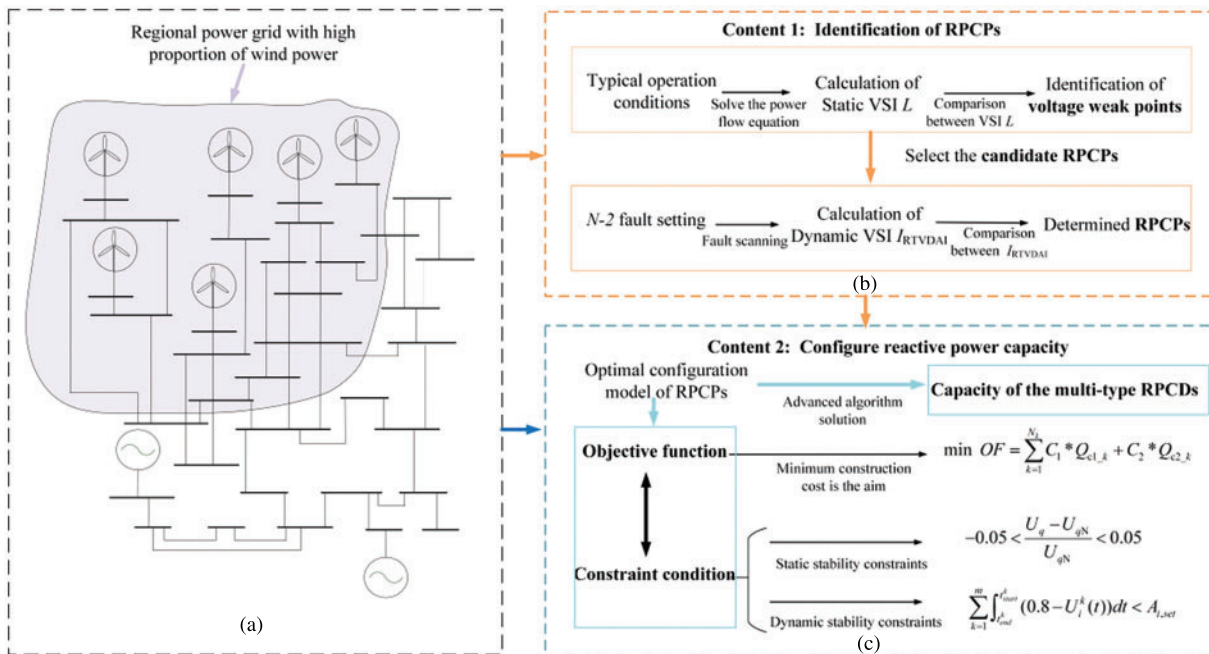
Figure 1: Schematic diagram of the overall strategy framework

The proposed method outlined in this paper entails a systematic approach to optimizing the allocation of RPCDs within transmission grids. Comprising two fundamental stages, this method begins with the meticulous selection of allocation points for RPCDs, followed by the allocation of

capacities for the chosen devices. These steps, crucial for enhancing grid stability and efficiency, are clearly delineated in Fig. 1b,c, providing a visual roadmap of the entire process.

To initiate the allocation process, weak voltage points within the grid are identified as potential candidate points based on the proposed static VSI under typical scenarios. Subsequently, a comprehensive evaluation is conducted through N-2 fault scanning on the lines connected to these weak voltage points, assessing their dynamic VSI. By integrating both static and dynamic considerations, the final reactive power compensation points (RPCPs) are determined. This meticulous selection process ensures the robust placement of RPCDs capable of effectively addressing voltage stability concerns across various operational scenarios.

Moving on to the capacity allocation stage, a multi-type reactive power compensation device optimization model is developed for the RPCPs. This model, designed to minimize construction costs while adhering to constraints related to both static and dynamic voltage stability, forms the crux of the capacity allocation process. Leveraging advanced optimization algorithms, the model facilitates the determination of optimal capacities for static and dynamic RPCDs. This ensures static voltage stability under typical operating conditions while providing substantial dynamic reactive power support during transient processes, thus enhancing the overall resilience of the transmission grid. Through the systematic implementation of these steps, the proposed method aims to pave the way for efficient and cost-effective integration of reactive power compensation devices, fostering a more sustainable and reliable energy infrastructure.

3 Voltage Operation Characteristics of Regional Power Grid with High Proportion of WP

Based on the operating principles of wind turbines, this chapter analyzes the influence mechanisms of grid-connected WP system on grid voltage. Additionally, considering the common RPCDs in regional power grids with high proportion of WP, the operational characteristics are elucidated through the mathematical models constructed for typical static and dynamic RPCDs.

3.1 Influence on Voltage Stability of Regional Power Grid for Intensive Access of WFs

Fig. 2 is a schematic diagram of the grid-connected WP system. In this figure, $\dot{U}_w$ is the terminal voltage of the WF unit, $\dot{U}_p$ is the voltage at the point of grid connection, $\dot{U}_g$ is the equivalent voltage of the system, R_w and X_w respectively represent the equivalent resistance and reactance of the transmission line and transformer in the WF, R_g and X_g respectively represent the equivalent resistance and reactance of the power grid. All relevant parameters have been converted to values consistent with the voltage level at the grid connection point.
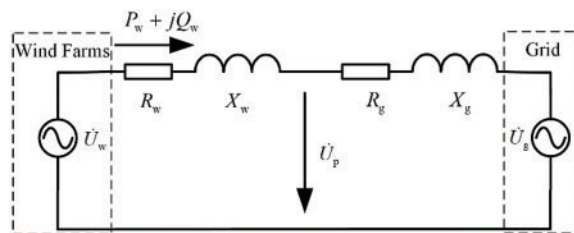

Figure 2: Schematic diagram of grid connection equivalent of WF

Taking the system equivalent voltage vector $\dot{U}_g$ as the reference axis, the following expression can be obtained from Fig. 2:

$$\dot{U}_w = U_g + \frac{P_w\left(R_w + R_g\right) + Q_w\left(X_w + X_g\right)}{U_w} + j\frac{P_w\left(X_w + X_g\right) - Q_w\left(R_w + R_g\right)}{U_w} \tag{1}$$

$$\dot{U}_p = U_w - \frac{P_w R_w + Q_w X_w}{U_w} - j\frac{P_w X_w - Q_w R_w}{U_w} \tag{2}$$

where P_w and Q_w represent the active power and reactive power output of the wind turbine, respectively.

Assuming the system is an infinite source, denoted by $\dot{U}_g$ as a constant. According to Eq. (1), when the change in wind causes the variations of the active power P_w and reactive power Q_w of the wind turbine, it causes the change in the terminal voltage $\dot{U}_w$ of the wind turbine. Moreover, according to Eq. (2), the change of terminal voltage $\dot{U}_w$ of the wind turbine will affect the voltage $\dot{U}_p$ of the grid connection point, resulting in the voltage change of each node.

In the voltage drop equation, the voltage amplitude difference is mainly determined by the longitudinal component of the voltage drop, while the phase angle difference of the voltage is determined by the transverse component. During WF operation, it is required to supply reactive power to the power grid in order to maintain a constant power factor. Therefore, according to Eq. (1), when the active power output P_w and reactive power output Q_w of the wind turbine change, the amplitude of the wind turbine terminal voltage $\dot{U}_w$ changes. Further according to Eq. (2), the amplitude of the voltage $\dot{U}_p$ at the junction point will also change, leading to alterations in the voltages at various nodes.

As the proportion of WP in the system continues to increase, the fluctuation characteristics of WP output will not only affect the voltage at the junction point, but also have a great impact on the voltage of each node in the grid system connected to the WF. Therefore, it is no longer applicable to use infinite power supply for equivalent value in the grid-connected system. If the infinite power grid in Fig. 2 evolves into a regular node with load, that is, $\dot{U}_g$ is no longer a constant. According to Eqs. (1) and (2), when the output P_w and Q_w of the WF change, the grid-connected voltage $\dot{U}_p$ of the WF and the voltage $\dot{U}_g$ of each node in the connected power grid system will change. If the RPCDs are not properly configured, it will seriously affect the safe and efficient grid connection of WFs.

3.2 Operation Characteristics of RPCDs

Due to the discrete nature of static RPCD during actual operation, preset switching commands are established during grid dispatch, hence their operational status typically affects the system's static voltage stability criteria. In contrast, dynamic RPCDs can output continuous reactive power based on predetermined reference voltage values during transient processes, thereby enhancing the system's dynamic voltage stability criteria. This section analyzes the operational characteristics of different types of reactive power compensation devices through the mathematical models of two typical devices.

Capacitor Bank (CB) and Static Synchronous Compensator (STATCOM) are selected as typical static RPCDs and dynamic RPCDs in this section, respectively. The working principles of each device are analyzed separately.

3.2.1 Capacitor Bank

The operation principle of CBs for reactive power compensation is based on their connection or disconnection to regulate the reactive power of system. When the CB is connected to the system, it can provide reactive power compensation; When it is disconnected, it does not provide reactive power

compensation. The expression for the reactive power output Q_{CB} of the CB is given by:

$$Q_{\text{CB}} = C_{\text{CB}} U_{\text{CB}}^2 * \omega \tag{3}$$

where C_{CB} is the total capacitance of the CB; U_{CB} is the voltage at both terminals of the CB; ω is the angular frequency of the grid.

CB, as the most widely used RPCD, has the advantages of wide adjustment range, low investment cost and high technical maturity. However, their discrete operational characteristics limit their flexibility and responsiveness in meeting the precise and rapid dynamic adjustment requirements of modern power systems during real-time operations.

3.2.2 STATCOM

STATCOM is a bridge converter made up of fully controllable power electronic components designed for dynamic RPCD applications. Leveraging power electronic devices, STATCOM demonstrates exceptionally rapid dynamic response capabilities, capable of addressing the system's reactive power demands within milliseconds. It enables precise control over both the magnitude and phase angle of the output voltage, allowing for accurate reactive power compensation in line with predefined reference values. The mathematical expression for the reactive power output of STATCOM is given by:

$$Q_{\text{STAT}} = -U_{\text{STAT}} I_{\text{STAT}} \sin\left(\delta_{\text{STAT}} - \theta_{\text{g}}\right) \tag{4}$$

where Q_{STAT} is the reactive power provided or absorbed by STATCOM; U_{STAT} is the output voltage amplitude of STATCOM; I_{STAT} is the output current amplitude of STATCOM; δ_{STAT} is the phase angle of the output voltage; θ_{g} is the phase angle of the grid voltage.

When the loss is ignored, the operational schematic diagram is shown in Fig. 2. Where $\dot{U}_{\text{g}}$ is the equivalent voltage of the power grid; $\dot{U}_{\text{STAT}}$ is the AC voltage output by STATCOM; $\dot{U}_L$ is the voltage on the reactor L. According to the Kirchhoff's Voltage Law (KVL), it follows that $\dot{U}_{\text{g}} = \dot{U}_{\text{STAT}} + \dot{U}_L$, I is the current flowing through the inductor, which corresponds to the current absorbed from the power grid. In the absence of consideration for the inverter and its own losses, there is no energy exchange between STATCOM and the power grid. Combining Eq. (4), it can be seen that as long as $\dot{U}_{\text{g}}$ and $\dot{U}_{\text{STAT}}$ remain in phase, changing the amplitude of the voltage $\dot{U}_{\text{STAT}}$ enables control over the magnitude and direction of the current I absorbed from the grid. The specific principle is illustrated in Fig. 3.
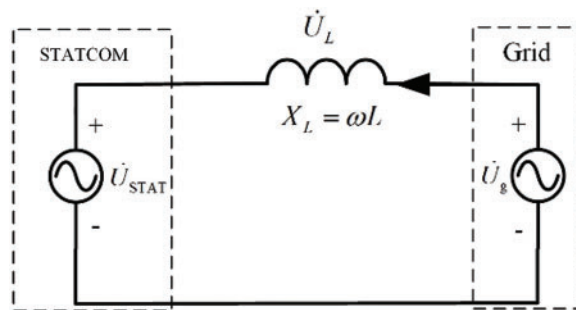

Figure 3: STATCOM grid-connected equivalent diagram

When $U_{\text{STAT}} < U_{\text{g}}$, the current lags behind the voltage by 90°. The load is inductive, absorbing inductive reactive power, as shown in Fig. 4a.

When $U_{\text{STAT}} > U_{\text{g}}$, the current leads the voltage by 90°. The load is capacitive, absorbing capacitive reactive power, as shown in Fig. 4b.

When $U_{\text{STAT}} = U_{\text{g}}$, the current and voltage are in phase. The load is resistive, not absorbing any reactive power, as shown in Fig. 4c.

(a) Capacitive reactive power condition

(b) Inductive reactive power condition

(c) Zero reactive power condition
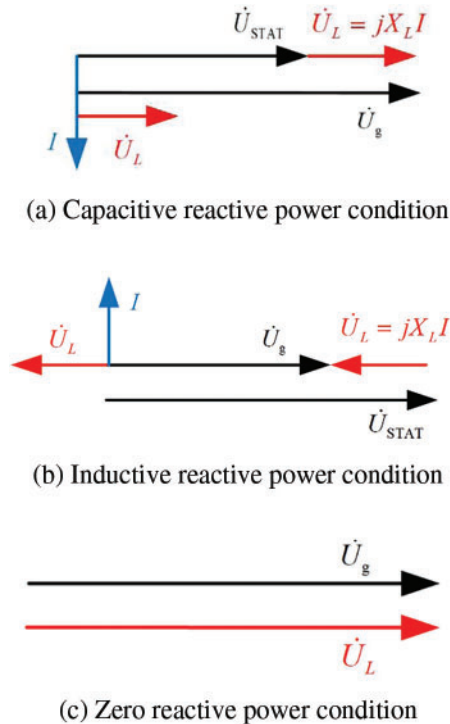
Figure 4: Phasor diagram of STATCOM grid-connected operation

4 Identification of RPCPs

Static VSI and dynamic VSI are proposed to identify RPCPs in this chapter. The specific logic is: static VSI of all nodes in the regional power grid can be calculated under the selected typical operation conditions, and the range of candidate points of RPCPs can be defined. Further, in order to analyze the voltage dynamic operation capability of the candidate points of the RPCPs, an N-2 fault scan is performed on the outgoing line of the target to be selected point, and the dynamic VSI of the target to be selected point is calculated to determine the configuration point of the reactive power compensation device. Its logical structure is shown in the Fig. 5.
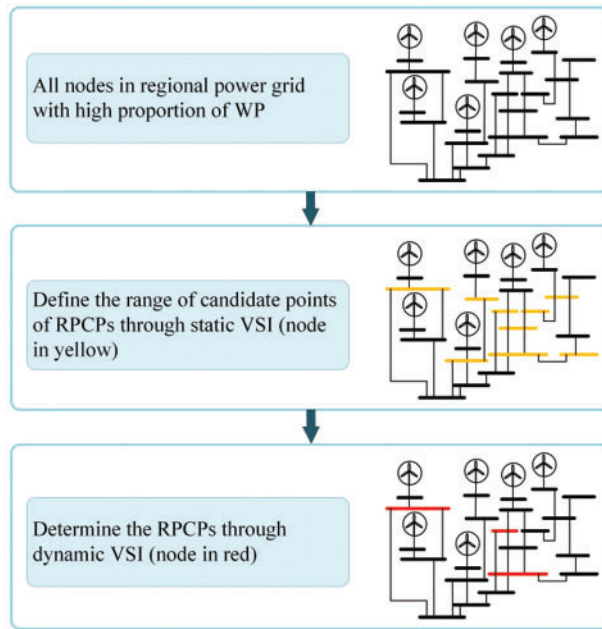
Figure 5: Diagram of the relationship between static VSI and dynamic VSI

4.1 Static VSI

In this paper, L_j is adopted as the static VSI under typical operation condition with high output of WF, which depends on the power flow calculation results under typical operation conditions. Therefore, the node admittance matrix of the system needs to be read and constructed to form the corresponding equation of state:

$$\begin{bmatrix} I_L \\ I_G \end{bmatrix} = \begin{bmatrix} Y_{LL} & Y_{LG} \\ Y_{GL} & Y_{GG} \end{bmatrix} \begin{bmatrix} U_L \\ U_G \end{bmatrix} \tag{5}$$

where I_G and U_G are the current vector and voltage vector of the injected power supply node, respectively; I_L and U_L are the current vector and voltage vector of the send-out nodes, respectively; Y_{LL} and Y_{GG} are self-admittance between the send-out nodes and injection power nodes, and Y_{LG} and Y_{GL} are mutual admittance between the send-out nodes and injection power nodes.

Solve the power flow equation under typical operation condition with high output of WF, and calculate the power flow distribution of each substation according to the power flow solution results. The equivalent output power expression of substation j is as follows:

$$\widetilde{S}_j = \sum_{a=1}^{A} P_a + jQ_a \tag{6}$$

where a is the send-out node connected to the j-th substation; A is the total number of send-out nodes connected to the j-th substation; $P_a + jQ_a$ is the power of the a-th send-out node.

The static VSI L of each substation of the WF grid-connected system is calculated by calculating the result of the power flow equation under typical operating conditions. Taking substation j as an example, the calculation expression of the static VSI L_j is as follows:

$$L_j = \frac{\left| \sum_{i \in \alpha_L} \frac{Z_{ij}^* \tilde{S}_i}{U_i} \right|}{|U_j|} \tag{7}$$

where U_i is the bus voltage vector of the i-th substation; $|U_j|$ is the bus voltage amplitude of substation j; Z_{ij}^* is the conjugation of the mutual impedance between substations; $\tilde{S}_i$ is the equivalent output power of the i-th substation of the system, i.e., $\tilde{S}_i = P_i + jQ_i$.

Based on the calculated VSI L of each substation, the average value L_{ave} of static VSI L of all substations is obtained, and the static VSI L of each substation is compared with the average value L_{ave}. If the static VSI L of the substation is greater than the average value L_{ave}, i.e., $L_j > L_{ave}$, it can be judged that the substation is the weak point of static voltage stability. The set m_L of weak point of static voltage stability is used as the reactive power compensation candidate point.

4.2 Dynamic VSI

The dynamic VSI is based on the area of dynamic voltage drop and is designed to compare the voltage support capabilities of various nodes during major disturbances, and it quantifies the extent to which voltage weak nodes affect other nodes. This paper takes N-2 fault as a typical large disturbance fault, and the schematic diagram of the N-2 fault disturbance of the line is shown in Fig. 6.
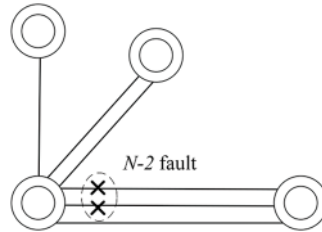
Figure 6: Schematic diagram of the N-2 fault disturbance of the line

Take voltage weak node j as an example, if there are M adjacent nodes of this node, and the node has a total of Q_N outgoing lines, scanning all the set N-2 faults, and calculating the dynamic voltage drop area $S_{\text{RTVDAI},j,t}$ of each adjacent node under each large disturbance condition, and the expression for the relative dynamic VSI $I_{\text{RTVDAI},j}$ can be obtained:

$$I_{\text{RTVDAI},j} = \max \{S_{\text{RTVDAI}}(1), S_{\text{RTVDAI}}(2), \ldots, S_{\text{RTVDAI}}(F)\} \tag{8}$$

where

$$S_{\text{RTVDAI},j}(f) = \sum_{i=1}^{M} S_{\text{RTVDAI},i} \tag{9}$$

where $S_{\text{RTVDAI},j}(f)$ is the dynamic voltage drop area of all adjacent nodes of the j-th static voltage stability weak point under fault f, M is the number of adjacent nodes of the static voltage stability weak point j, F is the number of check faults of the j-th static voltage stability weak point, $I_{\text{RTVDAI},j}$ is the maximum value of $S_{\text{RTVDAI},j}(f)$ under each check fault is taken.

When a certain N-2 fault occurs, the dynamic voltage drop area $S_{\text{RTVDAI},j,t}$ of the i-th adjacent node is calculated as follows:

$$S_{\text{RTVDAI},i} = \int_{t'_{start}}^{t'_{end}} (u_{i\_N} - u_i(t))\, dt \tag{10}$$

where $S_{\text{RTVDAI},i}$ is the dynamic voltage drop area of the i-th adjacent node under each N-2 fault disturbance condition, t'_{start} is the moment when the i-th adjacent node first experiences voltage drop to 80% of its rated value, t'_{end} is the moment when the voltage of the i-th adjacent node drops below or equal to 80% of its rated value and then recovers and remains above 80% of its rated value, U_{i_N} is the voltage rated value of the i-th adjacent node, and $u_i(t)$ is the voltage trajectory curve of the i-th node under the fault.

Based on the calculation method described above, the relative dynamic VSI $I_{\text{RTVDAI},j}$ is obtained for each reactive power compensation candidate point in the set m_L of static voltage weak nodes. This index is then sorted in descending order to form the set m_I, and finally the final RPCP can be determined based on actual planning demand.

5 Optimal Configuration Model of RPCD

5.1 Objective Function

The RPCP can be determined according to the static VSI and the dynamic VSI, and then the specific installed capacity of the static RPCD and the dynamic RPCD at each RPCP need to be determined, respectively. This chapter designs the optimal configuration model for the RPCDs that considers both static and dynamic voltage stability conditions.

As the construction cost of RPCDs is high, the proposed model aims to minimize the total construction cost of the RPCDs at each compensation point. The objective function is equated as follows:

$$\min OF = \sum_{k=1}^{N_k} C_1 * Q_{c1\_k} + C_2 * Q_{c2\_k} \tag{11}$$

where C_1 is the unit capacity construction cost of static RPCD; C_2 is the unit capacity construction cost of the dynamic RPCD; Q_{c1_k} is the capacity of static RPCD at the k-th point of reactive power compensation; Q_{c2_k} is the capacity of the dynamic RPCD at the k-th point of reactive power compensation; N_k is the total number of RPCPs.

5.2 Constraints

Static stability constraints consist of power flow constraint, node voltage constraint, RPCD capacity constraint under typical operation conditions, and dynamic stability constraints consist of dynamic voltage stability constraints under N-2 fault scanning.

5.2.1 Static Stability Constraints

Under static stability constraint, the capacity Q'_{c1_k} of the static RPCD and the capacity Q'_{c2_k} of the dynamic RPCD, as decision variables, need to satisfy the power flow constraint, node voltage constraint and capacity constraint of the RPCD under typical operation conditions. Among them, the power flow constraint under typical operation conditions of the high output of WF is:

$$\text{s.t.} = \begin{cases} P_p + \sum_{q \in \Phi_{(:,p)}} \left(P_{qp} - \frac{P_{qp}^2 + Q_{qp}^2}{U_q^2} R_{qp} \right) = \sum_{t \in \Phi_{(p,:)}} P_{pt}, \forall p \in \Psi \\ Q_p + \sum_{q \in \Phi_{(:,p)}} \left(Q_{qp} - \frac{P_{qp}^2 + Q_{qp}^2}{U_q^2} X_{qp} \right) = \sum_{t \in \Phi_{(p,:)}} Q_{pt}, \forall p \in \Psi \end{cases} \tag{12}$$

The power expression of the node under typical operation conditions of the high output of WF is as follows:

$$\begin{cases} P_p = P_{\text{w\_max}} \\ Q_p = P_{\text{w\_max}} \tan \theta_{\text{w}} \end{cases} \tag{13}$$

where the power expression of RPCP k is:

$$\begin{cases} P_p = P_k \\ Q_p = Q_k + Q'_{\text{c1\_}k} + Q''_{\text{c2\_}k} \end{cases} \tag{14}$$

where $\Phi_{(p,:)}$ and $\Phi_{(:,p)}$ are the branch sets where node p is at the beginning and ending ends, respectively; q is the power injection node; t is the power output node; ψ is the set of system AC nodes; U_q is the voltage of the q-th node; P_{qp} is the active power on the branch qp; Q_{qp} is the reactive power on the branch qp; R_{qp} is the equivalent resistance of the branch qp; X_{qp} is the equivalent reactance of the branch qp; P_p is the active power injected by the p-th node; Q_p is the reactive power injected by node p; $P_{\text{w\_max}}$ is the output data of WF under typical operation conditions of the high output of WF; θ_{w} is the power factor of WF; P_k is the active power injected by the k-th RPCP; Q_k is the original reactive power injected at the k-th RPCP; $Q'_{\text{c1\_}k}$ is the capacity of static RPCD configured at the k-th RPCP; $Q''_{\text{c2\_}k}$ is the capacity of the dynamic RPCD configured at the k-th RPCP.

where the power expression of each node is:

$$\begin{cases} P_p = P_{p1} - P_{p2} \\ Q_p = Q_{p1} - Q_{p2} \end{cases} \tag{15}$$

where P_{p1} is the active power output of the p-th node, P_{p2} is the active power load of the p-th node, Q_{p1} is the reactive power output of the p-th node, and Q_{p2} is the reactive power load of the p-th node.

The reactive power expression of the k-th RPCP:

$$Q_p = Q_k + Q_{\text{c1\_}k} \tag{16}$$

where Q_k is the original reactive power injected by the k-th node for reactive power compensation configuration.

According to the safe operation requirements of the power grid [35], and the system node voltage constraint expression is as follows:

$$-0.05 < \frac{U_q - U_{q\text{N}}}{U_{q\text{N}}} < 0.05 \tag{17}$$

where $U_{q\text{N}}$ is the operation voltage rating of the q-th node, and U_q is the operation voltage value of the q-th node.

The capacity constraint expression of the RPCD is:

$$Q_{\text{c1\_}k\_\text{min}} < Q_{\text{c1\_}k} < Q_{\text{c1\_}k\_\text{max}} \tag{18}$$

$$Q_{\text{c2\_}k\_\text{min}} < Q_{\text{c2\_}k} < Q_{\text{c2\_}k\_\text{max}} \tag{19}$$

where $Q_{c1\_k\_min}$ and $Q_{c1\_k\_max}$ are the lower limit and upper limit of the configured capacity of the static RPCD at the k-th RPCP; $Q_{c2\_k\_min}$ and $Q_{c2\_k\_min}$ are the lower limit and upper limit of the configured capacity of the dynamic reactive power compensation equipment at the k-th RPCP; Q_{c1_k} is the capacity of static RPCD configured at the k-th RPCP; Q_{c2_k} is the capacity of the dynamic RPCD configured at the k-th RPCP.

5.2.2 Dynamic Stability Constraints

Under the dynamic voltage stability constraints, the dynamic reactive power support capacity Q_{c2_k} in the dynamic RPCD, as a decision variable, needs to satisfy the dynamic voltage stability constraints. The specific implementation method involves scanning the N-2 faults in the outgoing lines of the reactive power compensation nodes, combined with its corresponding dynamic voltage drop area $S_{RTVDAI,j,t}$, and establish the dynamic voltage stability constraint under large disturbance:

$$\sum_{k=1}^{m} \int_{t^k_{end}}^{t^k_{start}} \left(0.8 - U^k_i(t)\right) dt < A_{i,set} \tag{20}$$

where $A_{i,set}$ is the threshold value of the critical transient voltage drop area of the i-th node, t^k_{start} is the moment when voltage drops to 0.8 p.u. for the k-th time of a fault, t^k_{end} is the moment when the voltage recovers to above 0.8 p.u. for the k-th time of a fault; $U^k_i(t)$ is the voltage trajectory curve of the i-th node for the k-th time of a fault when the voltage drops below 0.8 p.u.; m is the total number of curves with voltage below 0.8 p.u. under a certain fault.

The specific calculation method of $A_{i,set}$ is to conduct multi-type fault simulation on the i-th node in advance, and select the critical value of the maximum voltage drop area under the condition of voltage stability. The equation is as follows, where $A_{j,i,set}$ is the integral value of the voltage drop area under the j-th type of fault:

$$A_{i,set} = \max \left\{A_{1,i,set}, A_{2,i,set}, \cdots, A_{j,i,set}\right\} \tag{21}$$

5.3 Model Solving Based on PSO Algorithm

The optimal configuration model of RPCD built in Sections 5.1 and 5.2 is a typical optimization model with multiple decision variables and multiple constraints. Therefore, particle swarm optimization (PSO) algorithm is used in this section to solve the capacity of static RPCD and dynamic RPCD configured by RPCP.

The fundamental concept of the PSO algorithm is as follows: Firstly, determining the number of particles N and initializing their positions and velocities, while setting objective function. Secondly, establishing upper and lower limits for the positions and velocities of each particle. Next, computing the fitness of each particle. Subsequently, comparing the fitness of the current particle with its own historical best solution and the global best solution, updating both accordingly. Then, iterating to update the velocities and positions of particles according to the iteration formula. If the set target condition is not met, the process returns to the previous step, and the condition of ending the optimization process is generally to meet the convergence condition required by the model or to reach the set number of iterations.

The expression for updating the position and velocity of the particle based on the two related extreme values of the historical optimal solution and the global optimal solution is as follows:

$$x^{t+1}_{id} = x^t_{id} + v^{t+1}_{id} \tag{22}$$

$$v_{\text{id}}^{t+1} = w * v_{\text{id}}^{t} + c_1 * r_1 * \left(p_{\text{id}}^{t} - x_{\text{id}}^{t} \right) + c_2 * r_2 * \left(p_{\text{gd}}^{t} - x_{\text{gd}}^{t} \right) \tag{23}$$

where x_{id}^{t+1} is the particle position after iteration; v_{id}^{t+1} is the particle velocity after iteration; p_{id}^{t} is the historical optimal solution of the particle. p_{gd}^{t} is the global optimal solution; w is the inertia weight; c_1 and c_2 are acceleration factors. r_1 and r_2 are independent random numbers with the interval $[0,1]$. The flow chart of PSO algorithm is shown in Fig. 7.
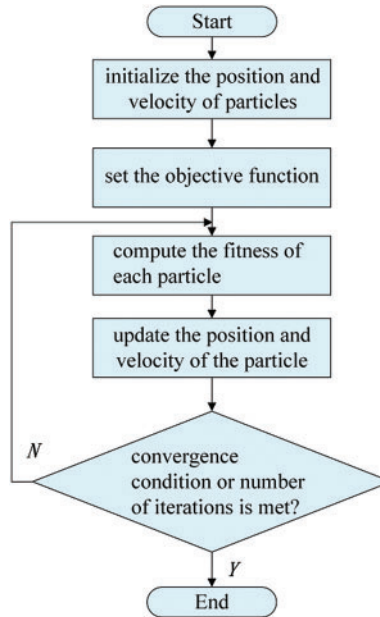
Figure 7: Flow chart of PSO algorithm

To apply the PSO algorithm to solve the capacity optimization model of RPCD constructed in this paper, the number of particle swarm initialization should be determined according to the number of RPCP, and the reactive power capacity of static RPCD and dynamic RPCD to be obtained should be taken as the optimization target, that is, the particle position in the PSO algorithm. In the optimization process, each decision variable in the iterated particle position set is put into the static stability constraint and the dynamic stability constraint to judge. If all constraints are met, the construction cost of RPCD under the decision variable is calculated by Eq. (11), and the process is iterated repeatedly until the target construction cost is met. In this case, the value of the decision variable is the reactive power capacity configured by RPCD.

6 Simulation Analysis

To validate the effectiveness of the proposed method in this paper, the modified 68 bus system is used as the research subject, and topological diagram is shown in Fig. 8. A corresponding system model is built in the PST toolbox of simulation software MATLAB. The system model consists of 68 nodes, including 16 generator nodes and 52 load nodes.
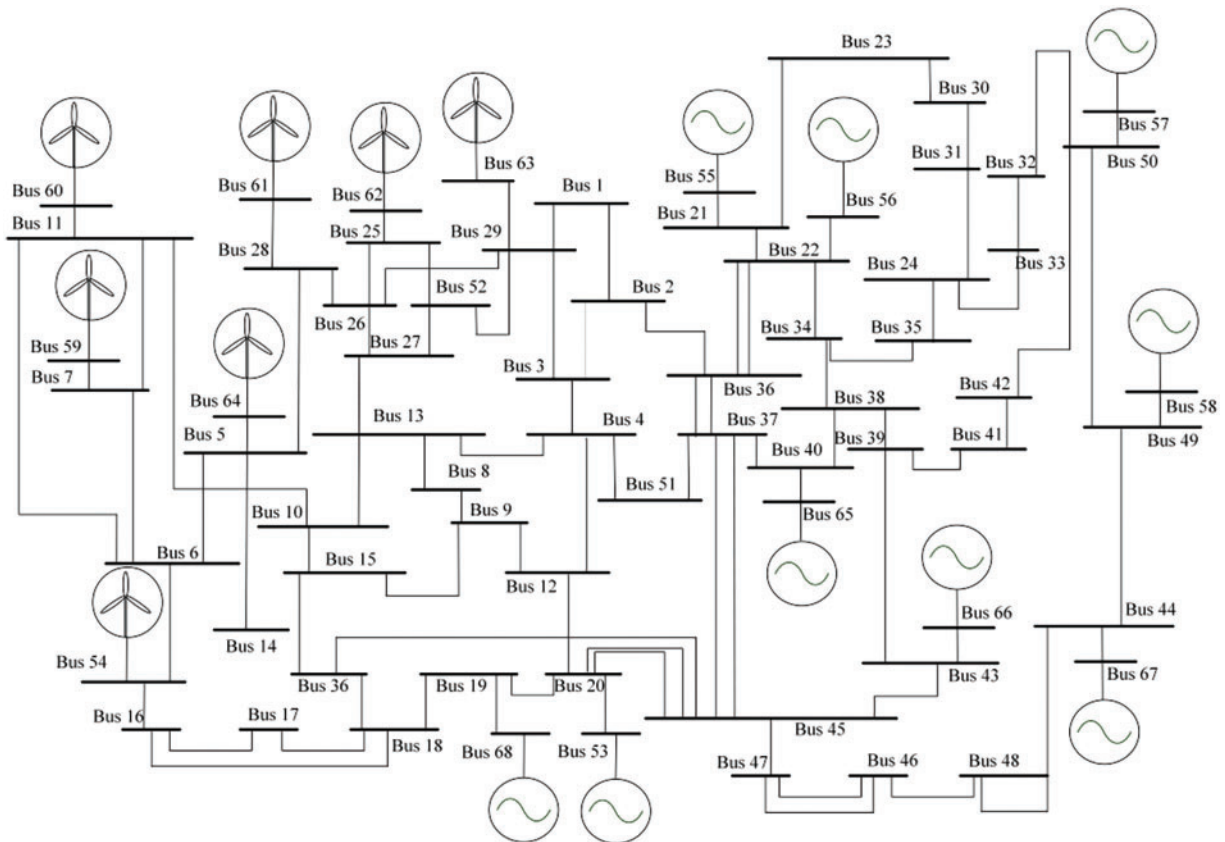
**Figure 8:** Topological diagram of modified 68 bus system

6.1 Identification of Reactive Power Compensation Configuration Points

#### 6.1.1 Selection of Static Voltage Weak Nodes

According to Eqs. (5) to (7) in Section 3.1, the static VSI L_j of each node in the system is calculated, and the calculation results are shown in Fig. 9. Calculate the average value L of static VSI L_{ave}, and compare the static VSI L_j of each node with L_{ave}. Nodes 6, 10, 20, 24, 26, 36, 37, 39, 40, 41, 42, 44, 45, 49, 50, 51, 52, 54, 59, 60, 61, 62, 63 are identified as static voltage weak nodes, which serve as the reactive power compensation candidate point. Specific values are given in the Table A1.

6.1.2 Calculation of Dynamic Voltage Drop Area of Voltage Weak Nodes

Perform N-2 fault scan for voltage weak nodes, and the system experiences a fault at 3.0 s. Based on Eqs. (8) and (10), calculate the dynamic voltage drop area index I_{RTVDAI} of voltage weak nodes. The calculation results of the dynamic voltage drop area index I_{RTVDAI} for voltage weak nodes, sorted in descending order, are summarized in Fig. 10. Specific values are given in the Table A2.
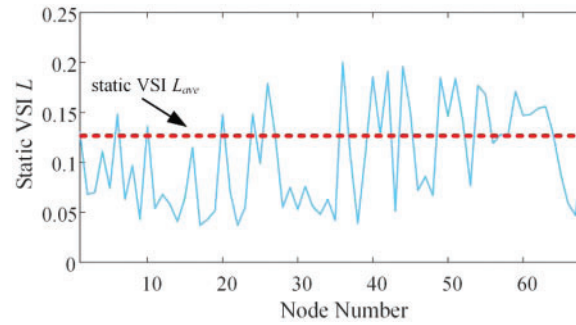
Figure 9: Statistical diagram of static VSI statistics
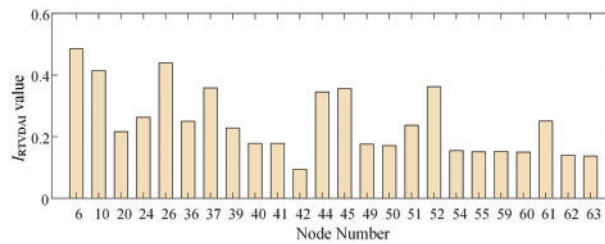
Figure 10: Statistical diagram of I_{RTVDAI} value of voltage weak nodes

Based on the descending order of the dynamic voltage drop area index I_{RTVDAI}, it is observed that the 6-*th*, 26-*th* and 10-*th* node have relatively high values. Therefore, these nodes from the set of voltage weak nodes are selected as for RPCPs. Performing an *N*-2 fault scan for the lines connected to the RPCPs, and the following uses the 6-*th* node as an example, the voltage dynamic operation curves of adjacent nodes for the RPCP are shown in Fig. 11.

It can be seen from the index calculation method mentioned in Section 4.2 and the dynamic operation curves of each weak node that the voltage stability weak node with more adjacent nodes has a larger dynamic voltage drop area index $I_{\text{RTVDAI},j}$, which can be used as the selected point for reactive power compensation.

6.2 Reactive Capacity Optimization of RPCDs

Using the reactive power optimal configuration model proposed in Sections 3.1 and 3.2, which considers both static and dynamic voltage stability, the capacities of the RPCDs are optimized for the selected RPCPs. The unit construction cost C_1 of the static RPCD is set at 8600 \$/MVar, and the unit construction cost C_2 of the dynamic RPCD is set at 24,800 \$/MVar.

In Section 5.3, it is proposed to solve the capacity optimization model of RPCD constructed by using PSO algorithm. Since three RPCPs are determined in Section 6.1, the particle swarm number *N* can be set to 15. At the same time, according to the capacity results of RPCD configured by bus nodes in the actual project, and let the initial capacity of the static RPCD and dynamic RPCD configured for the three nodes be 40 and 100 MVar. After optimization and solution by PSO algorithm, the capacity of static RPCD configured at the 6-*th* node, 26-*th* and 10-*th* node is 41 MVar, 55 MVar and 37 MVar, and the capacity of dynamic RPCD is 166, 109 and 87 MVar. The relevant statistics are provided in Table 1.
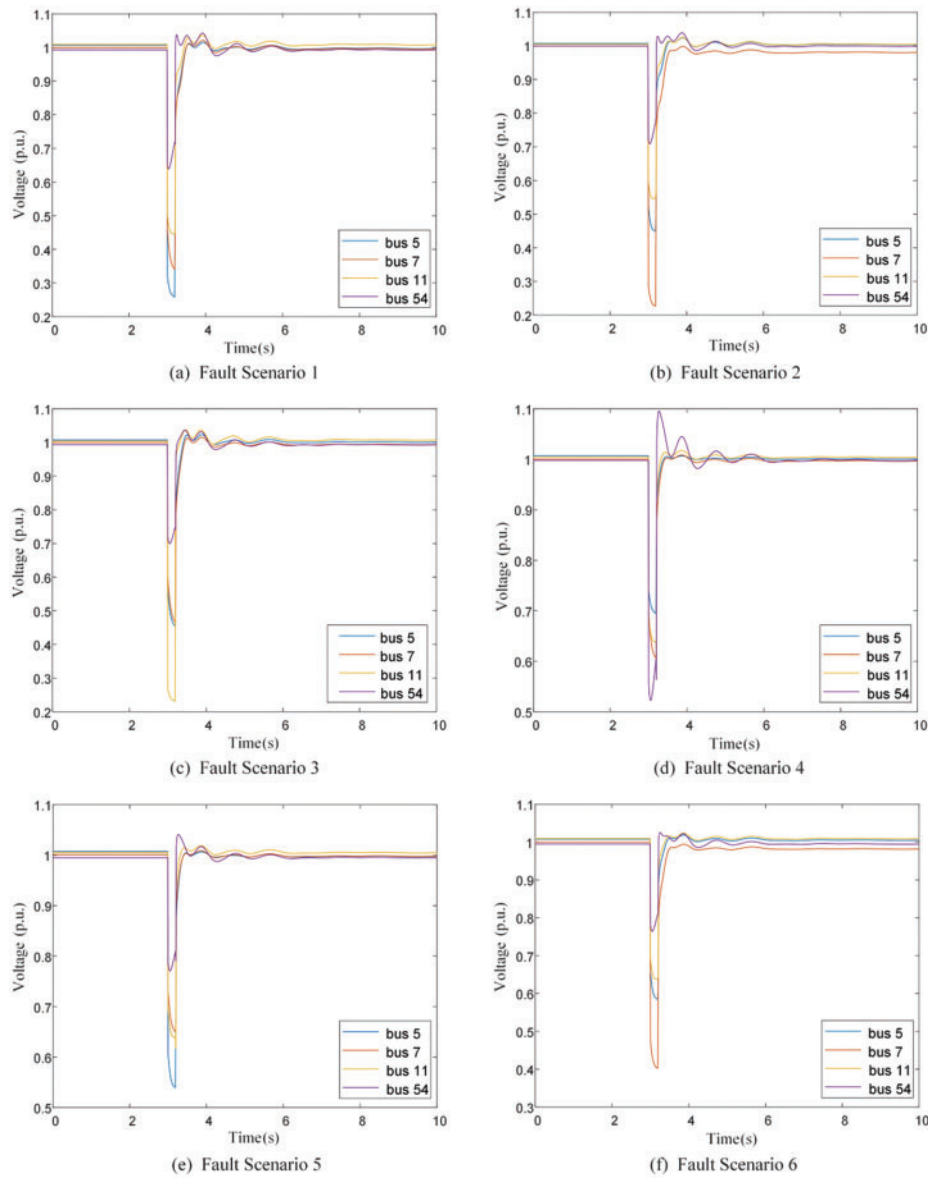
Figure 11: Voltage dynamic operation curve of adjacent nodes of the 6-*th* node

Table 1: Capacity configuration statistics of RPCD

RPCPs	Static reactive power compensation capacity (MVar)	Dynamic reactive power compensation capacity (MVar)	Static reactive power compensation cost (M$)	Dynamic reactive power compensation cost (M$)	Total cost (M$)
6-*th* node	41	166	35.2	411.7	446.9
26-*th* node	55	109	37.4	270.3	307.7
10-*th* node	37	87	31.8	215.7	247.5

According to the solution results of the proposed optimization model, the capacity of the static RPCD configured at each RPCP is obtained. The power flow equations are solved for the same typical scenario, and based on the power flow results, it is found that during steady-state operation, the voltage at the 6-*th* node increases from 0.946 to 1.009 p.u., the voltage at the 10-*th* node increases from 0.937 to 1.018 p.u., and the voltage at the 26-*th* node increases from 0.939 to 1.026 p.u. after the optimization configuration. The voltage performance of every node has seen significant enhancements, with a comparison of the static voltage operation shown in Fig. 12. It should be noted that high nodes are nodes of power supply or nodes that are far away from the regional power grid in the dense access areas of new energy stations, so under typical working conditions, the voltage change of high nodes is small.
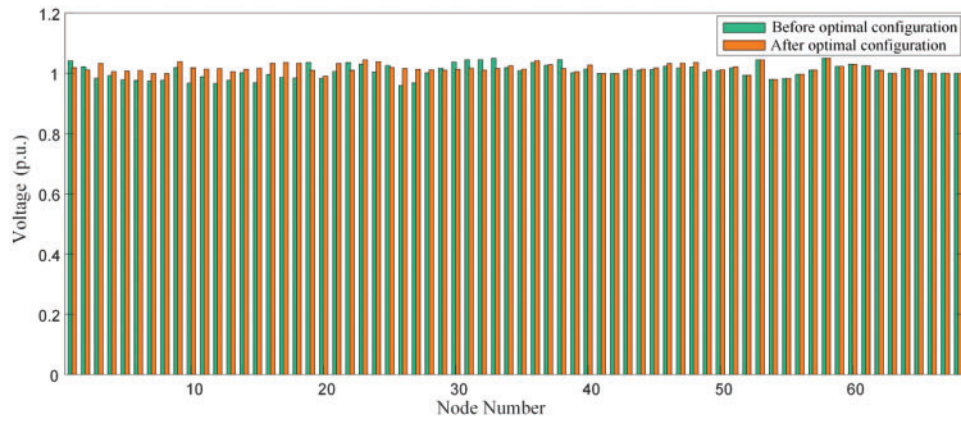

Figure 12: Comparison of static voltage operation of each node

In addition, in order to highlight the voltage operation problem faced by the research object in the calculation example, in this example, RPCDs are assumed to be configured at the grid-connected point of WF to ensure voltage stability. As can be seen from the figure, the 40-*th* to 68-*th* node are the grid-connected points of the power source or nodes far away from the regional power grid with a high proportion of WP. Therefore, under typical working conditions, the voltage variation of these nodes is small.

Taking the most common single-phase short circuit fault in practical operation as a typical fault, single-phase short circuit faults with a grounding resistance of 0.1Ω is set at the RPCP to analyze the voltage dynamic characteristics of each node and adjacent nodes before and after the optimization configuration of RPCDs. The following uses the 6-*th* node as an example, Fig. 13 below respectively shows the voltage operation curves of the 6-*th* node during the occurrence of typical faults.

It can be observed that configuration of RPCDs at the voltage weak nodes significantly improves the voltage dynamic characteristics of the originally weak nodes. The lowest voltage drop point is elevated, and the operation voltage is restored to 0.8 p.u. in a shorter time. Additionally, the dynamic characteristics of the adjacent nodes of the configured RPCD nodes are also improved.
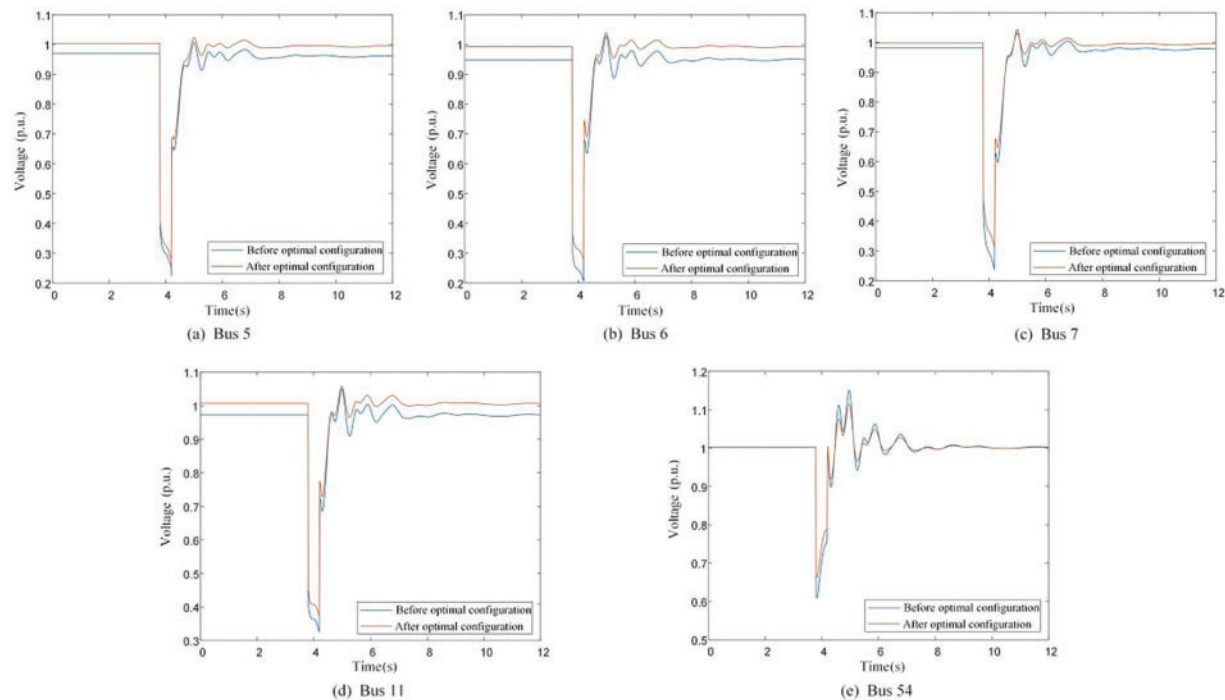
Figure 13: Dynamic operation curves of relevant nodes of the 6-*th* node under typical fault

7 Conclusion

This paper presents an optimal configuration method for multi-type RPCDs in regional power grids with a high proportion of wind power. The proposed method systematically identifies the location and determines the capacity of the required RPCDs for a regional power grid model that facilitates intensive access to WFs. It enhances the operational capacity of voltage-weak nodes in the system and ensures static and dynamic voltage stability in regional power grids with a high proportion of WP. Moreover, this method exhibits high economic efficiency, and it is deemed as a crucial support for achieving large-scale grid-connected WFs.

It is important to note that the proposed method for identifying voltage weak nodes based on VSI considers a limited range of typical operational conditions. Additionally, the optimization configuration model for RPCDs solely considers construction costs without factoring in the operational costs of RPCDs and the regulation capabilities of different types of RPCDs. Addressing these deficiencies will be the primary focus of future research.

Author Contributions: The authors confirm contribution to the paper as follows: study conception and design: Ying Wang, Cangbi Ding; data collection: Jie Dang, Chenyi Zheng; analysis and interpretation

of results: Ying Wang, Yi Tang; draft manuscript preparation: Ying Wang, Cangbi Ding. All authors reviewed the results and approved the final version of the manuscript.

Ethics Approval: Not applicable.

Availability of Data and Materials: Not applicable.

Conflicts of Interest: The authors declare that they have no conflicts of interest to report regarding the present study.

References

[1] A. Z. A. Shaqsi, K. Sopian, and A. Al-Hinai, "Review of energy storage services, applications, limitations, and benefits," *Energy Rep.*, vol. 6, no. 5, pp. 288–306, Dec. 2020. doi: 10.1016/j.egyr.2020.07.028.

[2] Y. Hao, D. Su, and Z. Lei, "Optimal intelligence planning of wind power plants and power system storage devices in power station unit commitment based," *Energy Eng.*, vol. 119, no. 5, pp. 2081–2104, Jul. 2022. doi: 10.32604/ee.2022.021342.

[3] L. Wang, Z. Wang, Y. Yang, S. Zhou, Y. Dong and F. Zhang, "Review on wind power development and relevant policies between China and Japan," *Energy Eng.*, vol. 118, no. 6, pp. 1611–1626, Sep. 2021. doi: 10.32604/EE.2021.016010.

[4] X. Zhou, C. Ding, J. Dai, Z. Li, Y. Hu and Z. Qie, "An active power coordination control strategy for AC/DC transmission systems to mitigate subsequent commutation failures in HVDC systems" *Electronics*, vol. 10, no. 23, pp. 3044, Dec. 2021. doi: 10.3390/electronics10233044.

[5] S. Sun, P. Yu, J. Xing, Y. Cheng, S. Yang and Q. Ai, "Short-term wind power prediction based on ICEEMDAN-SE-LSTM neural network model with classifying seasonal," *Energy Eng.*, vol. 120, no. 12, pp. 2761–2782, Nov. 2023. doi: 10.32604/ee.2023.042635.

[6] I. D. Margaris, S. A. Papathanassiou, N. D. Hatziargyriou, A. D. Hansen, and P. Sorensen, "Frequency control in autonomous power systems with high wind power penetration," *IEEE Trans. Sustain. Energy,* vol. 3, no. 2, pp. 189–199, Apr. 2012. doi: 10.1109/TSTE.2011.2174660.

[7] L. Xiang, H. Zhu, Y. Zhang, Q. Yao, and A. Hu, "Impact of wind power penetration on wind-thermal-bundled transmission system," *IEEE Trans. Power Electron.*, vol. 37, no. 12, pp. 15616–15625, Dec. 2022. doi: 10.1109/TPEL.2022.3189366.

[8] M. Bakhtvar and A. Keane, "Allocation of wind capacity subject to long term voltage stability constraints," *IEEE Trans. Power Syst.*, vol. 31, no. 3, pp. 2404–2414, May 2016. doi: 10.1109/TPWRS.2015.2454852.

[9] S. Nikkhah and A. Rabiee, "Optimal wind power generation investment, considering voltage stability of power systems," *Renew. Energy*, vol. 115, pp. 308–325, Jan. 2018. doi: 10.1016/j.renene.2017.08.056.

[10] W. Bao, L. Ding, Z. Liu, G. Zhu, M. Kheshti and Q. Wu, "Analytically derived fixed termination time for stepwise inertial control of wind turbines—Part I: Analytical derivation," *Int. J. Electr. Power Energy Syst.*, vol. 121, pp. 1–10, Oct. 2020.

[11] F. Xiao *et al.*, "The short-term prediction of wind power based on the convolutional graph attention deep neural network," *Energy Eng.,* vol. 121, no. 2, pp. 359–376, Jan. 2024. doi: 10.32604/ee.2023.040887.

[12] B. Chen, F. Miao, J. Yang, C. Qi, and W. Ji, "A temporary frequency response strategy using a voltage source-based permanent magnet synchronous generator and energy storage systems," *Energy Eng.*, vol. 121, no. 2, pp. 541–555, Jan. 2024. doi: 10.32604/ee.2023.028327.

[13] H. Zhang, C. Li, Q. Wei, and Y. Zhang, "Fault detection and diagnosis of the air handling unit via combining the feature sparse representation based dynamic SFA and the LSTM network," *Energy Build.,* vol. 269, no. 4, pp. 112241, Aug. 2022. doi: 10.1016/j.enbuild.2022.112241.

[14] T. F. Megahed, E. F. Morgan, P. N. Timo, and M. Saeed, "Neural network predictive control for fault detection and identification in DFIG with SMES for low voltage ride-through requirements," *Ain Shams Eng. J.*, vol. 15, no. 7, pp. 102775, Apr. 2024. doi: 10.1016/j.asej.2024.102775.

[15] X. Ge, J. Qian, Y. Fu, W. J. Lee, and Y. Mi, "Transient stability evaluation criterion of multi-wind farms integrated power system," *IEEE Trans. Power Syst.*, vol. 37, no. 4, pp. 3137–3140, July 2022. doi: 10.1109/TPWRS.2022.3156430.

[16] H. Zhang, W. Yang, W. Yi, J. B. Lim, Z. An and C. Li, "Imbalanced data based fault diagnosis of the chiller via integrating a new resampling technique with an improved ensemble extreme learning machine," *J. Build. Eng.*, vol. 70, no. 2, pp. 106338, July 2023. doi: 10.1016/j.jobe.2023.106338.

[17] A. Boričić, J. L. R. Torres, and M. Popov, "Fundamental study on the influence of dynamic load and distributed energy resources on power system short-term voltage stability," *Int. J. Electr. Power Energy Syst.*, vol. 131, no. 2, pp. 107141, Oct. 2021. doi: 10.1016/j.ijepes.2021.107141.

[18] S. Munikoti, B. Natarajan, K. Jhala, and K. Lai, "Probabilistic voltage sensitivity analysis to quantify impact of high PV penetration on unbalanced distribution system," *IEEE Trans. Power Syst.*, vol. 36, no. 4, pp. 3080–3092, Jul. 2021. doi: 10.1109/TPWRS.2021.3053461.

[19] B. Ismail, N. I. Abdul Wahab, M. L. Othman, M. A. M. Radzi, K. Naidu Vijyakumar and M. N. Mat Naain, "A comprehensive review on optimal location and sizing of reactive power compensation using hybrid-based approaches for power loss reduction, voltage stability improvement, voltage profile enhancement and loadability enhancement," *IEEE Access*, vol. 8, pp. 222733–222765, 2020. doi: 10.1109/ACCESS.2020.3043297.

[20] E. Vittal, M. O'Malley, and A. Keane, "A steady-state voltage stability analysis of power systems with high penetrations of wind," *IEEE Trans. Power Syst.*, vol. 25, no. 1, pp. 433–442, Feb. 2010. doi: 10.1109/TPWRS.2009.2031491.

[21] B. B. Adetokun, C. M. Muriithi, and J. O. Ojo, "Voltage stability assessment and enhancement of power grid with increasing wind energy penetration," *Int. J. Electr. Power Energy Syst.*, vol. 120, no. 2, pp. 105988, Sep. 2020. doi: 10.1016/j.ijepes.2020.105988.

[22] J. Then, A. P. Agalgaonkar, and K. M. Muttaqi, "Hosting capacity of an australian low-voltage distribution network for electric vehicle adoption," *IEEE Trans. Ind. Appl.*, vol. 60, no. 2, pp. 2601–2610, Mar.–Apr. 2024. doi: 10.1109/TIA.2023.3337068.

[23] H. Zaheb *et al.*, "A contemporary novel classification of voltage stability indices," *Appl. Sci.*, vol. 10, no. 5, pp. 1639, Feb. 2020. doi: 10.3390/app10051639.

[24] Y. Li, Q. Chen, L. Wu, Y. Yan, and J. Zhou, "Wind farm reactive power demand analysis based on sensitivity and stability constraints considering wind speed fluctuations," *IEEE Trans. Power Syst.*, vol. 36, no. 2, pp. 1465–1477, Sep. 2020.

[25] S. Tamalouzt *et al.*, "Enhanced direct reactive power control-based multi-level inverter for DFIG wind system under variable speeds," *Sustainability,* vol. 13, no. 16, pp. 9060, Aug. 2020. doi: 10.3390/su13169060.

[26] J. Ouyang, T. Tang, J. Yao, and M. Li, "Active voltage control for DFIG-based wind farm integrated power system by coordinating active and reactive powers under wind speed variations," *IEEE Trans. Energy Convers.,* vol. 34, no. 3, pp. 1504–1511, Sep. 2019. doi: 10.1109/TEC.2019.2905673.

[27] Y. Guo, H. Gao, Q. Wu, H. Zhao, J. Østergaard, and M. Shahidehpour, "Enhanced voltage control of VSC-HVDC-connected offshore wind farms based on model predictive control," *IEEE Trans. Sustain. Energy,* vol. 9, no. 1, pp. 474–487, Jan. 2018. doi: 10.1109/TSTE.2017.2743005.

[28] Y. Li, S. Zhang, Y. Li, J. Cao, and S. Jia, "PMU measurements-based short-term voltage stability assessment of power systems via deep transfer learning," *IEEE Trans. Instrum. Meas.*, vol. 72, pp. 1–11, Sep. 2023. doi: 10.1109/TIM.2023.3311065.

[29] T. Liu, X. Gu, S. Li, Y. Bai, T. Wang and X. Yang, "Static voltage stability margin prediction considering new energy uncertainty based on graph attention networks and long short-term memory networks," *IET Renew. Power Gener.*, vol. 17, no. 9, pp. 2290–2301, May 2023. doi: 10.1049/rpg2.12731.

[30] Y. Zhou, Z. Li, and G. Wang, "Study on leveraging wind farms' robust reactive power range for uncertain power system reactive power optimization," *Appl. Energy*, vol. 298, no. 4, pp. 117130, Sep. 2021. doi: 10.1016/j.apenergy.2021.117130.

[31] Y. Liu, D. Ćetenović, H. Li, E. Gryazina, and V. Terzija, "An optimized multi-objective reactive power dispatch strategy based on improved genetic algorithm for wind power integrated systems," *Int. J. Electr. Power Energy Syst.*, vol. 136, no. 4, pp. 107764, Mar. 2022. doi: 10.1016/j.ijepes.2021.107764.

[32] N. Gupta, "Probabilistic optimal reactive power planning with onshore and offshore wind generation, EV, and PV uncertainties," *IEEE Trans. Ind. Appl.*, vol. 56, no. 4, pp. 4200–4213, Jul.–Aug. 2020.

[33] A. Radaideh, M. M. Bodoor, and A. Al-Quraan, "Active and reactive power control for wind turbines based DFIG using LQR controller with optimal gain-scheduling," *Electr. Comput. Eng.*, vol. 2021, no. 5, pp. 1–19, Oct. 2021. doi: 10.1155/2021/1218236.

[34] N. Wang, J. Li, W. Hu, B. Zhang, Q. Huang, and Z. Chen, "Optimal reactive power dispatch of a full-scale converter based wind farm considering loss minimization," *Renew. Energy*, vol. 139, no. 2, pp. 292–301, 2019. doi: 10.1016/j.renene.2019.02.037.

[35] North American Electric Reliability Corporation, "Reliability guideline," 2018. Accessed: Mar. 20, 2024. [Online]. Available: https://www.nerc.com/comm/RSTC_Reliability_Guidelines/Inverter-Based_Resource_Performance_Guideline.pdf

Appendix A

Table A1: Static VSI statistics

Number	L_j value	Number	L_j value	Number	L_j value	Number	L_j value
1	0.105	19	0.052	37	0.078	55	0.168
2	0.068	20	0.148	38	0.039	56	0.119
3	0.07	21	0.071	39	0.078	57	0.128
4	0.111	22	0.037	40	0.136	58	0.127
5	0.074	23	0.055	41	0.093	59	0.171
6	0.148	24	0.148	42	0.063	60	0.147
7	0.063	25	0.099	43	0.051	61	0.148
8	0.097	26	0.179	44	0.065	62	0.154
9	0.043	27	0.128	45	0.110	63	0.156
10	0.136	28	0.055	46	0.072	64	0.129
11	0.054	29	0.075	47	0.086	65	0.089
12	0.068	30	0.053	48	0.067	66	0.059
13	0.058	31	0.076	49	0.135	67	0.047
14	0.041	32	0.056	50	0.146	68	0.124
15	0.065	33	0.048	51	0.184		
16	0.115	34	0.063	52	0.103		
17	0.037	35	0.042	53	0.077		
18	0.043	36	0.067	54	0.177		

Table A2: Dynamic voltage drop area index of voltage weak nodes

Weak node	I_{RTVDAI} value	Weak node	I_{RTVDAI} value
6	0.825	20	0.216
26	0.539	41	0.178
10	0.474	40	0.178
52	0.362	49	0.176
37	0.358	50	0.171
45	0.356	54	0.155
44	0.345	59	0.152
24	0.263	55	0.151
61	0.251	60	0.150
36	0.250	62	0.140
51	0.237	63	0.137
39	0.228	42	0.094